Received: 23 May 2019 | Revised: 26 September 2019 | Accepted: 5 November 2019

DOI: 10.1111/gbi.12371

ORIGINAL ARTICLE

gebiology WILEY

The microbially driven formation of siderite in salt marsh sediments

Chin Yik Lin[1,2] | Alexandra V. Turchyn[1] | Alexey Krylov[3,4,5] | Gilad Antler[6,7]

[1]Department of Earth Sciences, University of Cambridge, Cambridge, UK

[2]Department of Geology, Faculty of Science, University of Malaya, Kuala Lumpur, Malaysia

[3]VNIIOkeangeologia, St. Petersburg, Russia

[4]Institute of Earth Sciences, St Petersburg State University, St. Petersburg, Russia

[5]Limnological Institute, SB RAS, Irkutsk, Russia

[6]Department of Geological and Environmental Sciences, Ben-Gurion University of the Negev, Beersheba, Israel

[7]The Interuniversity Institute for Marine Sciences in Eilat, Eilat, Israel

Correspondence
Chin Yik Lin, Department of Earth Sciences, University of Cambridge, Cambridge, UK.
Emails: chinyik85@gmail.com; chinyik@um.edu.my

Funding information
Skim Latihan Akademik IPTA (SLAI) Scholarship; H2020 European Research Council, Grant/Award Number: ERC StG 307582 to AVT

Abstract

We employ complementary field and laboratory-based incubation techniques to explore the geochemical environment where siderite concretions are actively forming and growing, including solid-phase analysis of the sediment, concretion, and associated pore fluid chemistry. These recently formed siderite concretions allow us to explore the geochemical processes that lead to the formation of this less common carbonate mineral. We conclude that there are two phases of siderite concretion growth within the sediment, as there are distinct changes in the carbon isotopic composition and mineralogy across the concretions. Incubated sediment samples allow us to explore the stability of siderite over a range of geochemical conditions. Our incubation results suggest that the formation of siderite can be very rapid (about two weeks or within 400 hr) when there is a substantial source of iron, either from microbial iron reduction or from steel material; however, a source of dissolved iron is not enough to induce siderite precipitation. We suggest that sufficient alkalinity is the limiting factor for siderite precipitation during microbial iron reduction while the lack of dissolved iron is the limiting factor for siderite formation if microbial sulfate reduction is the dominant microbial metabolism. We show that siderite can form via heated transformation (at temperature 100°C for 48 hr) of calcite and monohydrocalcite seeds in the presence of dissolved iron. Our transformation experiments suggest that the formation of siderite is promoted when carbonate seeds are present.

KEYWORDS

calcite, mineralogy, nodule, siderite, sulfate-reducing bacteria, transformation

1 | INTRODUCTION

Carbonate minerals are one of the major components of the sedimentary rock record. While the vast majority of carbonate rocks comprise the minerals calcite ($CaCO_3$), aragonite ($CaCO_3$), and dolomite ($CaMg(CO_3)_2$), other carbonate minerals, such as siderite ($FeCO_3$) can also be common (Baker, Kassan, & Hamilton, 1995; Konhauser et al., 2017). Siderite forms under certain unusual environmental conditions, often linked to changes in pH, changes in pCO_2, or changes in microbial metabolism (Dong, 2010; Konhauser, Newman, & Kappler, 2005; Van Lith, Warthmann, Vasconcelos, & McKenzie, 2003; Sanchez-Roman et al., 2014; Sanchez-Roman, Puente-Sanchez, Parro, & Amils, 2015; Xiouzhu, Unfei, & Huaiyan, 1996). In particular, the presence of siderite in the geological record has been used as an environmental indicator for conditions at Earth's surface (e.g., levels of atmospheric pCO_2 and O_2, redox conditions, and iron cycling) at various points in

Earth history, especially during the Archean Eon and Proterozoic Eon (Bachan & Kump, 2015; Canfield et al., 2018; Halevy, Alesker, Schuster, Popovitz-Biro, & Feldman, 2017; Holland, 2006; Konhauser et al., 2017; Ohmoto, Watanabe, & Kumazawa, 2004; Planavsky et al., 2018).

The formation of siderite, however, requires very particular environmental conditions. Siderite can only form under anoxic conditions due to the need for reduced, ferrous/dissolved or iron (Fe^{2+}) to react with carbonate ion (CO_3^{2}); dissolved iron is rapidly oxidized in the presence of oxygen (Bachan & Kump, 2015). The presence of hydrogen sulfide also precludes the formation of siderite because hydrogen sulfide reacts rapidly with dissolved iron to make iron monosulfide minerals and ultimately pyrite (Berner, 1981). However, the presence of dissolved iron is not the only factor needed to make siderite, the presence of dissolved inorganic carbon (DIC) is also needed. We note that often the measurement of DIC is not as straightforward as the measurement of alkalinity (or the solution's charge balance), which in many natural environments is largely carbonate alkalinity ($[HCO_3^-] + 2^*[CO_3^{2-}]$). In this paper, we will refer exclusively to alkalinity, as a broad proxy for the amount of DIC available for siderite formation in a solution or in the natural environment.

In addition to a source of dissolved iron and a source of alkalinity, to form siderite the pH needs to be between 6.0 and 7.2. A pH lower than 6 means carbonate precipitation will be significantly delayed, and if the pore fluid pH is greater than 7.2, precipitation of calcite or aragonite is favored (Roberts et al., 2013). The formation of siderite is often assumed to involve microbially mediated chemical reactions, such as bacterial iron reduction, that produce dissolved iron and generate alkalinity through the oxidation of organic carbon (Baumann, Birgel, Wargreich, & Peckmann, 2016; Van Lith et al., 2003; Roberts et al., 2013; Sel, Radha, Dideriksen, & Navrotsky, 2012). However, bacterial iron reduction alone tends to push the pH of the pore fluid higher than 7.2 (Soetaert, Hofmann, Middleberg, Meysman, & Greenwood, 2007; Zeng & Tice, 2014), which means that for siderite to form, more is needed than simply local conditions that favor bacterial iron reduction.

Studies involving the microbially induced precipitation of siderite via anoxic incubation of sediment, that is, batch culture, are difficult because if the system progresses past bacterial iron reduction to microbial sulfate reduction, any dissolved iron will react with aqueous hydrogen sulfide and will no longer be available to make siderite. Microbially induced precipitation of siderite has been reported using pure culture of *Geobacter metallireducens*, a bacterial iron reducer, in the laboratory (Mortimer, Coleman, & Rae, 1997). Zachara et al. (1998) also found that *Shewanella putrefaciens*, CN32, a bacterium that can reduce either iron or manganese oxides, was able to reduce iron oxides and lead to the precipitation of vivianite and siderite. Replicating these in batch cultures with natural abundances of multiple microbial populations has been challenging. Furthermore, the nucleation pathway for siderite is unclear, for example, whether there is a less stable carbonate precursor to siderite such as amorphous calcium carbonate (ACC), amorphous iron (II) carbonate (AFC) (Dideriksen et al., 2015; Jiang & Tosca, 2019; Sel et al., 2012) or monohydrocalcite (MHC) and whether siderite (both nodular or laminated) is then made during the transformation of these precursors to stable phases in the presence of dissolved iron. Understanding this mechanism for siderite formation may provide insights as to how changes in fluid chemistry impact the formation of various carbonate polymorphs during non-classical nucleation in an iron-dominated system and what environmental or biological conditions can be indicated by the presence of nodular/spheroidal and laminated siderite in the geological record. We note that siderite concretions are rarely pure siderite and often contain a mixture of carbonate mineral phases including an abundant amount of siderite; similarly, the siderite concretions in this study are only dominantly siderite and contain varying amounts of other phases. Nonetheless, they are broadly referred to as "siderite concretions."

Studies in a natural environment with modern siderite concretions could be a good analog to explore the environmental conditions under which siderite concretions may nucleate and grow. Nucleation of siderite during sedimentary diagenesis has been suggested to be a key pathway for formation of siderite in both modern (Vuillemin et al., 2019; Wittkopp, Teranes, Lubenow, & Dean, 2014) and ancient (Heimann et al., 2010) environments. In these studies, siderite nucleation in sediment influences the crystal morphology and conditions of growth. What is interesting is that if diagenetic siderite formation is the dominant pathway to form siderite concretions, then they may reflect conditions within the sediment column rather than conditions related to the overall ocean–atmosphere system. Hence, study of the formation of siderite in the laboratory and in the natural environment will allow us to better understand both the occurrences of siderite and to infer the influence of diagenesis on laminated and nodular siderite in the modern and ancient environments.

While there are studies looking at crystal morphology and isotopic composition of modern and ancient siderites (Abdul Hadi & Astin, 1995; Allison & Pye, 1994; Baumann et al., 2016; Moore, Ferrell, & Aharon, 1992; Raiswell & Fisher, 2000; Wittkop et al., 2014), and separate studies trying to nucleate siderite biotically or abiotically in the laboratory (Köhler, Konhauser, Papineau, Bekker, & Kappler, 2013; Mortimer, Galsworthy, Bittrell, Wilmot, & Newton, 2011; Mortimer & Coleman, 1997; Sanchez-Roman et al., 2015), there are few studies that couple the analysis of modern siderite to laboratory experiments trying to grow it. In the East Anglian salt marshes (particularly along the north Norfolk coast, in the salt marshes named Warham, Stiffkey, and Blakeney), there are large siderite concretions (up to 20 cm in diameter) found actively growing in the sediment (Figure 1). Despite some early studies exploring the mineralogy and solid-phase geochemistry of the siderite concretions in these salt marsh sediments, there has been less attention paid to the interplay between the microbes and aqueous geochemistry that leads to the precipitation of siderite (Allison & Pye, 1994; Coleman, Hedrick, Lovley, White, & Pye, 1993; Pye, 1984; Pye, Dickinson, Schiavon, Coleman, & Cox, 1990). Previous studies attribute the formation and growth of siderite concretions to high rates of "bacterial activity,' high organic matter content, tidal pumping, and high sedimentation rate (Baumann et al., 2016; Coleman, 1993; Pye, 1984; Pye et al., 1990). In this study, we examine the mineralogy and elemental

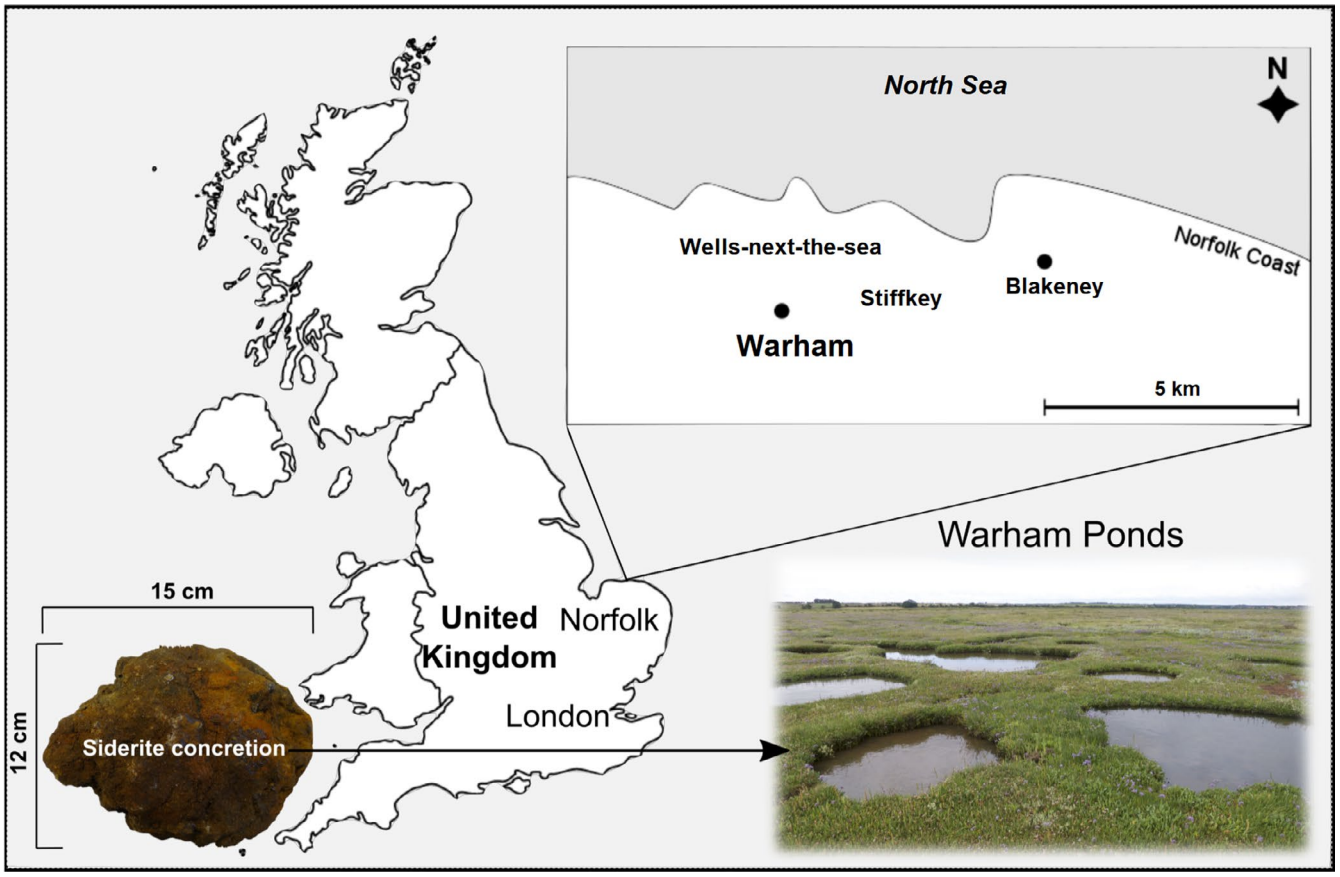

FIGURE 1 The location of East Anglian salt marshes along the coast of North Norfolk. Siderite concretions are found in sediment, ponds, and creeks of the Warham salt marsh. Sediment samples studied were collected from both Warham and Blakeney salt marshes

distributions of siderite concretions collected from the East Anglian salt marsh sediment, particularly those of the Warham salt marshes, to better understand the geochemical conditions during concretion nucleation and subsequent growth. We couple this field-based work to laboratory incubation experiments where we try to understand the environmental conditions under which siderite may precipitate and if there are precursors to siderite formation, for example, other carbonate phases that may transform to siderite and what the nucleation pathway might be. This study provides insight into the formation of siderite in marine environments (where sulfate is abundant) and may have important implications for paleoenvironmental interpretations (such as ancient seawater chemistry and the plausible conditions to form marine siderite beds).

2 | SIDERITE STABILITY IN THE EAST ANGLIAN SALT MARSH SEDIMENT

2.1 | Mineral saturation state in the sedimentary pore fluids

Here, we introduce the geochemical characteristics of the sediment and the distribution of concretions in the East Anglian salt marshes. Beneath the salt marsh platform, there are high concentrations of pore fluid dissolved iron (up to 5mM) (Hutchings et al., 2019). The salt marsh sediment mainly comprises quartz, orthoclase, albite, kaolinite, and talc, as suggested by XRD analysis (Appendix S1). Across the salt marsh platform, which are transected by tidal creeks, there are also small ponds, known as "salt ponds" or "salt pans." Two geochemically distinct sediment types are found beneath the salt ponds; the geochemistry of these two types of sediment has been reported extensively in previous publications (Antler, Mills, Hutchings, Redeker, & Turchyn, 2019; Hutchings et al., 2019; Mills, Antler, & Turchyn, 2016). One type of pond sediment has high pore fluid concentrations of aqueous hydrogen sulfide (up to 8mM), and the other type has high concentrations of aqueous dissolved iron (up to 2mM). Previous studies have explored the drivers behind the differing geochemical conditions (Antler et al., 2019; Hutchings et al., 2019; Mills et al., 2016). Based on our field observations, the siderite concretions are found in various places throughout the salt marsh sediment, growing both beneath the salt marsh platform, near the edge of the tidal creeks, and occasionally in the dissolved iron-rich pond sediment.

Based on the previously published pore fluid profiles from the North Norfolk pond sediments, we can calculate the stability of various mineral phases as a first estimate of where siderite is

supersaturated (Figure 2a, b redrew from Hutchings et al., 2019). To do this, we use PHREEQC (SIT database) to calculate the concentration of dissolved inorganic carbon (DIC) from the measured alkalinity and pH, and then use this to calculate the saturation index. This calculation suggests that the pore fluid in the iron-rich core is in equilibrium with respect to siderite and undersaturated with respect to calcite, aragonite, and dolomite (Figure 2). In the sulfidic sediment, we calculate that the porewater is slightly undersaturated with respect to calcite, aragonite, and siderite, although dolomite and rhodochrosite are oversaturated. One of the interesting initial observations is that siderite is not supersaturated in either the iron-rich or sulfide-rich pond sediment, suggesting that siderite concretions may nucleate or grow in other parts of the salt marsh platform than beneath the salt ponds where they can be found.

3 | MATERIALS AND METHODS

3.1 | Field sampling

All fresh siderite concretions were collected from the Warham salt marsh, found buried in the sediment in the vicinity of salt marsh ponds. Siderite concretions are also found in tidal creeks that bisect the salt marsh. Concretions were wrapped with mud in the field and sealed with polyethylene bags to minimize desiccation. In the laboratory, concretions were cut in half (Figure 3), one half is used for analysis and the other half was refrigerated.

3.2 | Analysis of concretions

For mineralogical analysis, fresh concretions were ground to powder using agate mortar and pestle before X-ray diffraction (XRD). X-Ray fluorescence (XRF) was performed using an Avaatech X-ray fluorescence core scanner at the University of Cambridge in 1- to 4-mm measurement intervals to obtain semi-quantitative elemental data of concretions. XRF scanning was conducted at a 60-s scanning rate with energy level of 10 kV (no filter) for Ca, S, and 30 kV (Pd filter) for Fe and Sr. All mineralogical data for XRD were collected in Bragg-Brentano geometry on a D8 Bruker diffractometer equipped with primary Gobbel mirrors for parallels Cu Kα X-rays and a Vantec position sensitive linear detector. Collection conditions were 15–70° in 2θ, 0.02 step size, 450 s/step, and divergence slits 0.6 mm. Rietveld refinements were performed with software Topas 4.1 (Coelho, 2007) to quantify the various mineral phases in the samples. Rietveld quantitative analysis is known to be unreliable for minor phases (<5 wt %). The accuracy is considered to be ± 1%–2% relative for major phases, while the estimated standard deviation (e.s.d.) from the Rietveld calculation has no bearing on the accuracy or otherwise of the quantification itself, it is merely related to the mathematical fit of the model (Madsen & Scarlett, 2008).

Bulk samples for carbon isotope analysis ($\delta^{13}C_{carbonate}$) were drilled from the center to the edge of the concretion. Between 50 and 200 micrograms of dried homogenized sample was transferred into exetainer vials and sealed with silicone rubber septa using a screw cap. The samples were flushed with chemically pure grade helium then acidified with 104% orthophosphoric acid, left to react for one hour at 70 ˚C, and then analyzed using a Thermo GasBench attached to a Thermo Delta V Advantage mass spectrometer in continuous flow mode. Each run of samples was accompanied by 10 reference carbonates (Carrara Z) and two control samples (Fletton Clay). Carrara Z has been calibrated to VPDB using the international standard NBS19 (TS-Limestone). The results are reported with reference to the international standard VPDB, and the analytical precision is better than ± 0.08 ‰ for $\delta^{13}C$.

3.3 | Incubation experiment with pure Norfolk salt marsh sediment

Sediment was incubated in an experiment we have named "W" using fresh sediment samples from the salt marshes. The goal of the incubation was to explore the evolution of aqueous chemistry and the precipitation of carbonate minerals in an environment that mimics the salt marsh subsurface sediment. In incubation experiment W, 10 cm^3 of the Warham sediment was used (Table 1). Four samples were set up which includes two replicates and two controls. Diluted seawater (50% seawater with 50% deionized water) was used as the medium to mimic the solution in the surface of the salt marsh ponds (Hutchings et al., 2019; Mills et al., 2016). Sodium acetate was added to the media to make up a concentration of approximately 10 mM; this is both the electron and carbon donors. Two steel balls (5 mm in diameter) and 0.4–0.5 g of wood were included in the incubated samples to serve as a nucleus for carbonate mineral precipitation. The steel balls and wood were buried in the sediment in both replicates and one of the controls. The other control sample contained only the medium and a steel ball, without sediment, to examine how much iron is abiotically released into the solution from the steel ball. Then, the reaction vessels were sealed and degassed with 90% N_2/10% CO_2 mixed gas for 5 min. All control samples were autoclaved twice to eliminate biological activities.

3.4 | Aqueous sample analysis

Aqueous samples were syringe filtered (0.2 μm), and pH was measured at 25°C on the NBS scale using an Orion 3 Star meter with ROSS micro-electrode (ORION 8,220 BNWP PerpHect ROSS—platinum wire as a reference in iodine/potassium iodide solution, ROSS internal filling solution is 3M KCl). Alkalinity was titrated potentiometrically with 0.1 M of HCl using a Metrohm 848 Titrino plus with an error of 2.5%. The HCl used for titrations was standardized with certified reference material (CRM) 2.2298 mEq/L. The CRM batch #157 used was provided by A.G. Dickson of Scripps Institution of Oceanography (Dickson, Afghan, & Anderson, 2003). Dissolved iron in the samples was fixed by ferrozine solution

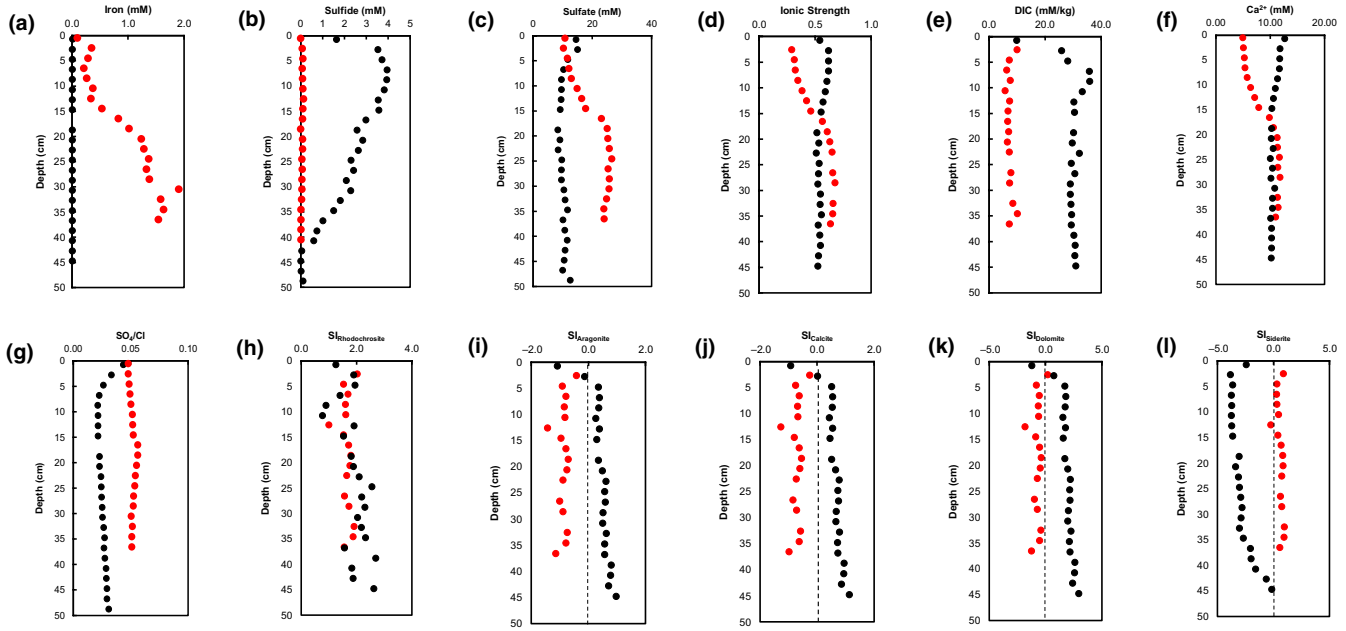

FIGURE 2 Geochemical data collected and previously published from the core of different types of ponds, red for iron rich pond and black for sulfidic pond. Pore-fluid profiles for (a) iron; (b) sulfide; (c) sulfate; (d) ionic strength; (e) dissolved inorganic carbon; (f) calcium; (g) SO4/Cl; (h) SIrhodochrosite; (i) SIaragonite; (j) SIcalcite; (k) SIdolomite; and (l) SIsiderite. Saturation indices (SI) of various minerals in the salt-marsh. If SI < −0.2, the pore-fluid is undersaturated with respect to that particular mineral. While SI = −0.2 ≤ 0 ≥ 0.2, it means that the pore fluid is in equilibrium with that mineral. If SI > 0.2, this indicates that the pore fluid is oversaturated with respect to that mineral. Iron and sulfide concentration data (Figure 2a,b) were redrawn from previously published data in Hutchings et al. (2019)

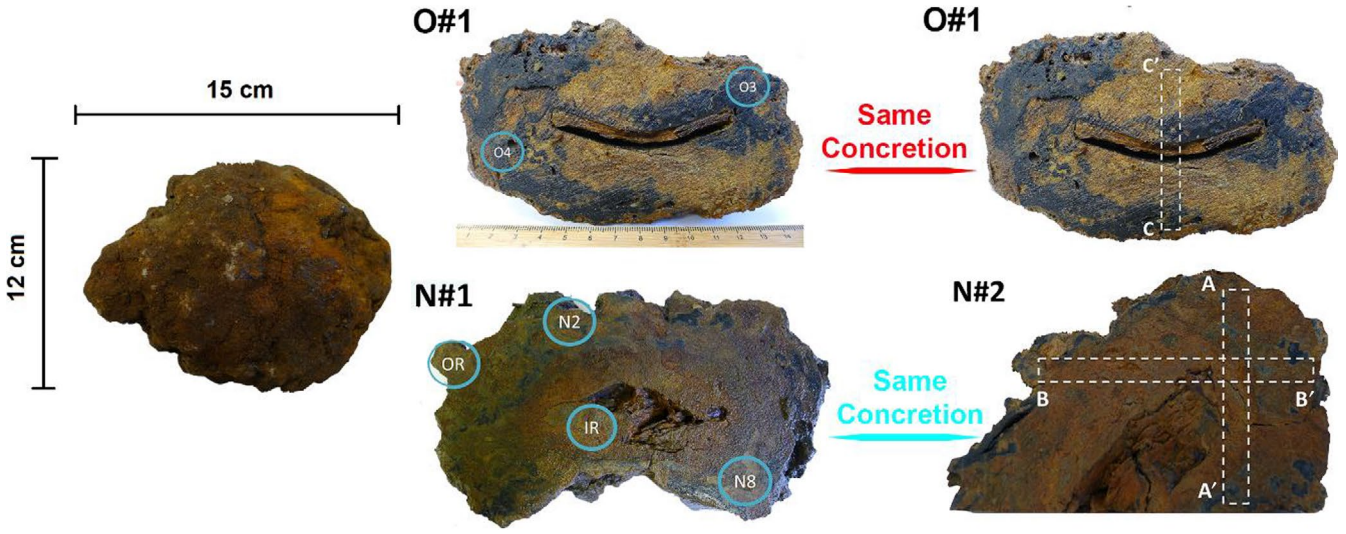

FIGURE 3 Two carbonate/siderite concretions (O and N—N#1 and N#2 are opposite halves of the same concretion) with diameter ~ 15 cm were cut in half for mineralogical and geochemical analysis. For mineralogical analysis, different parts of the concretion (blue circle) were extracted manually and pulverized prior to analyzing by XRD. To examine the bulk geochemical composition across the concretions (12-mm dotted line box of A-A' and B-B'—from N#2 and C-C'—from O#1), freshly cut samples were scanned by an Avaatech XRF core scanner

($C_{20}H_{13}N_4NaO_6S_2H_2O_{(s)}$, MW = 510.48 g/mol) prior to quantification using an Aqua-mate Plus UV-Vis Spectrophotometer at λ = 562 nm (Stookey, 1970). Aqueous sulfide was fixed with 0.05 M zinc acetate and spectrophotometrically measured using the methylene blue method at a wavelength of 670 nm (Cline, 1969). Samples for sulfate measurement were diluted 20 times before measured using ion chromatography on a Dionex ICS-5000$^+$ HPIC (through an anion IonPac AS18 column using 31mM of potassium hydroxide as eluent). Calibration standards were prepared by dilution of OSIL Atlantic Seawater standard (2%–10%) solution.

TABLE 1 Summary of the materials and setup in incubation experiments W

Incubation samples	Sediment source	Medium	Electron donors	Gas	Nucleation materials	Note
Incubation experiment W						
Replicate 1	Warham	Diluted seawater	Acetate	90% N_2/10% CO_2	Two steel balls, wood	50% strength seawater
Replicate 2	Warham	Diluted seawater	Acetate	90% N_2/10% CO_2	Two steel balls, wood	50% strength seawater
Killed control (without sediment)	None	Diluted seawater	Acetate	90% N_2/10% CO_2	One steel ball	50% strength seawater
Killed control (with sediment)	Warham	Diluted seawater	Acetate	90% N_2/10% CO_2	Two steel balls, wood	50% strength seawater

TABLE 2 Summary of the initial media and mineral seeds used in the transformation experiments. Samples with varying iron concentrations were labeled as medium in the initial and followed by the concentration of iron in millimolar. For example, MQ50 indicate the medium is MQ water with 50 mM of iron. SW denotes seawater as the medium. Samples MQ100–SW10 were incubated under anoxic condition to make sure ferrous iron is in its dissolved form. Initial $CaCO_3$ with MHC/Calcite indicates that the initial media is incubated with MHC or calcite

Samples	pH	Alk (mEq/L)	Ca^{2+} (mM)	Mg^{2+}(mM)	Fe^{2+}(mM)	PO_4^{3-}(μM)	SO_4^{2-}(mM)	Mg/Ca	Medium	Initial $CaCO_3$
MQ50*	3.02	1.780	<0.01	<0.01	50.55	-	-	-	M.Medium	MHC/Calcite
SW50*	3.65	1.625	10.80	55.36	53.64	-	-	5.13	M.Medium	MHC/Calcite
MQ100[a]	2.67	2.450	<0.01	<0.01	98.57	-	B.D.L	-	M.Medium	MHC/Calcite
MQ50[b]	3.02	8.278	<0.01	<0.01	50.63	-	B.D.L	-	M.Medium	MHC/Calcite
MQ25[c]	3.39	7.301	<0.01	<0.01	25.78	-	B.D.L	-	M.Medium	MHC/Calcite
MQ10[d]	7.20	13.283	<0.01	<0.01	11.03	-	B.D.L	-	M.Medium	MHC/Calcite
SW100[e]	2.97	3.979	10.41	53.12	105.04	-	22.07	5.10	M.Medium	MHC/Calcite
SW50[f]	4.33	5.158	10.53	53.98	48.74	-	17.68	5.12	M.Medium	MHC/Calcite
SW25[g]	5.20	6.503	10.49	52.91	23.67	-	23.68	5.04	M.Medium	MHC/Calcite
SW10[h]	6.78	12.948	10.83	54.75	9.74	-	-	5.05	M.Medium	MHC/Calcite

Note: MHC/Calcite indicates that the initial $CaCO_3$ seeds for transformation are MHC and calcite. Both MHC and calcite were incubated in separate vials. M.Medium is modified medium. B.D.L. indicates below detection limit.

*Samples incubated under oxic condition.

[a–d] = modified MQ water.

[e–h] = modified SW medium.

3.5 | Transformation experiment

To investigate the transformation of calcite and MHC into siderite, MHC precipitated from previous pure culture incubation experiments (Lin et al., 2018) was placed in different aqueous solutions of seawater and modified media (Table 2). Approximately 0.02 g of either or both MHC and calcite seeds (Sigma-Aldrich, ACS reagent, ≥ 99.0%, powder—Lot #MKBP1684V, CAS: 471-34-1) was heated under different media in sealed bottles at 100°C for 48 hr (Liu et al., 2013; Munemoto & Fukushi, 2008). Control samples were run without either MHC or calcite seeds. For samples with dissolved iron in the modified media, the media was degassed with N_2 for 10 min in a 5-ml vial. The solution was analyzed for pH, alkalinity, iron, major cations, and anions before and after the transformation experiment. Solid-phase samples were collected, dried, and analyzed for their morphology and mineralogy using *SEM* and XRD (mentioned above), respectively. The dried samples from both the incubation and transformation experiments were analyzed by field emission scanning electron microscopy (FESEM—QEMSCAN 650F FEI) equipped with an energy dispersive X-ray (EDX) detector to determine the morphology and chemical composition of the precipitates. The solid samples were placed on ultra-smooth carbon tape and sputter-coated with submicron layer (~10 nm) of carbon prior to *SEM* analysis.

4 | RESULTS

4.1 | Concretion mineralogy and geochemistry

Four out of five concretions collected from the Warham salt marsh nucleate around wood; one does not have a visible nucleus (which is not considered in this study). In this study, we selected two concretions to be analyzed for their geochemistry (sample names O and N). The concretions are black in color when freshly opened. No clear inner core or outer core, or central laminations, can be seen in either of these concretions (O and N) (Figure 3). Laminations only become

TABLE 3 Weight percentages of phases for concretion samples with relative estimated standard deviation e.s.d. (in parenthesis). Additional samples collected from the concretions (not shown in Figure 3) were homogenized and analyzed in bulk. Abbreviation of the samples is given in the Table's footnote

Sample	Quartz	Siderite	Mg-Calc	Greigite	Orthoclase	Albite	Gypsum	Pyrite	Dolomite	R_{wp}	χ^2
IR (*N*#1)	86.7 (±1.6)%	-	-	-	-	-	13.3 (±1.6)%	-	-	40.06	1.57
N2 (*N*#1) B	40.8 (±1.3)%	-	47.2 (±1.6)%	-	8.2 (±2.5)%	-	-	-	3.8 (±0.9)%	9.30	1.81
N8 (*N*#1) Br	60.5 (±2.5)%	14.0 (±1.4)%	5.4 (±1.5)%	6.1 (±1.4)%	14.0 (±2.6)%	-	-	<0.1 (±0.8)%	-	4.33	1.35
OR (*N*#1)	32.0 (±0.9)%	6.6 (±0.8)%	36.1 (±1.2)%	2.7 (±0.7)%	3.2 (±1.5)%	13.1 (±1.2)%	6.4 (±0.8)%	-	-	6.21	1.59
N#SB (OB)	43.9 (±1.0)%	-	49.8 (±1.2)%	-	-	6.3 (±1.5)%	-	-	-	9.49	2.77
N#SB	53.0 (±1.3)%	-	47.0 (±1.3)%	-	-	-	-	-	-	10.50	3.35
PWood (*N*#1)	40.5 (±2.7)	56.8 (±3.4)%	2.7* (±5.1)%	-	-	-	-	-	-	2.42	1.24
N#MBr	35.3 (±1.2)%	7.2 (±0.8)%	25.6 (±1.3)%	-	9.1 (±1.9)%	18.8 (±1.6)%	4.0 (±0.7)%	-	-	5.39	1.96
N#SB1	46.6 (±2.9)%	9.7 (±1.6)%	10.0 (±2.4)%	-	11.2 (±3.6)%	21.8 (±2.7)%	0.7 (±1.4)%	-	-	6.47	3.08
N#SBr1	46.5 (±2.0)%	10.5 (±1.2)%	-	-	5.0 (±2.5)%	32.3 (±1.9)%	5.4 (±1.0)%	-	-	4.90	2.39
O6 (Bulk)	46.0 (±1.7)%	26.4 (±1.2)%	10.3 (±1.4)%	-	5.6 (±1.9)%	9.4 (±2.1)%	2.3 (±0.9)%	-	-	4.58	2.06
O7 (Bulk)	45.8 (±2.5)%	17.8 (±1.4)%	5.6 (±2.1)%	-	12.8 (±3.0)%	15.5 (±2.3)%	-	-	2.5 (±1.7)%	7.72	3.31
O3 (O#1) B	72.6 (±1.1)%	27.4 (±1.1)%	-	-	-	-	-	-	-	5.02	1.52
O4 (O#1) Br	78.7 (±3.8)%	-	-	-	12.9 (±3.3)%	5.9 (±2.5)%	-	2.5 (±1.5)%	-	6.30	2.08
O#SB	59.1 (±0.9)%	-	40.9 (±0.9)%	-	-	-	-	-	-	8.19	2.60

Abbreviation of samples: O = sample O#1 (dark shaded); *N* = sample *N*#1 (light shaded); *M* = inner core of the concretion; S = edge of the concretions; B = black color region; Br = brownish/reddish colored region; Pwood = region next to wood material in *N*#1; O6 and O7 = bulk samples collected at random place of the sample O#1.

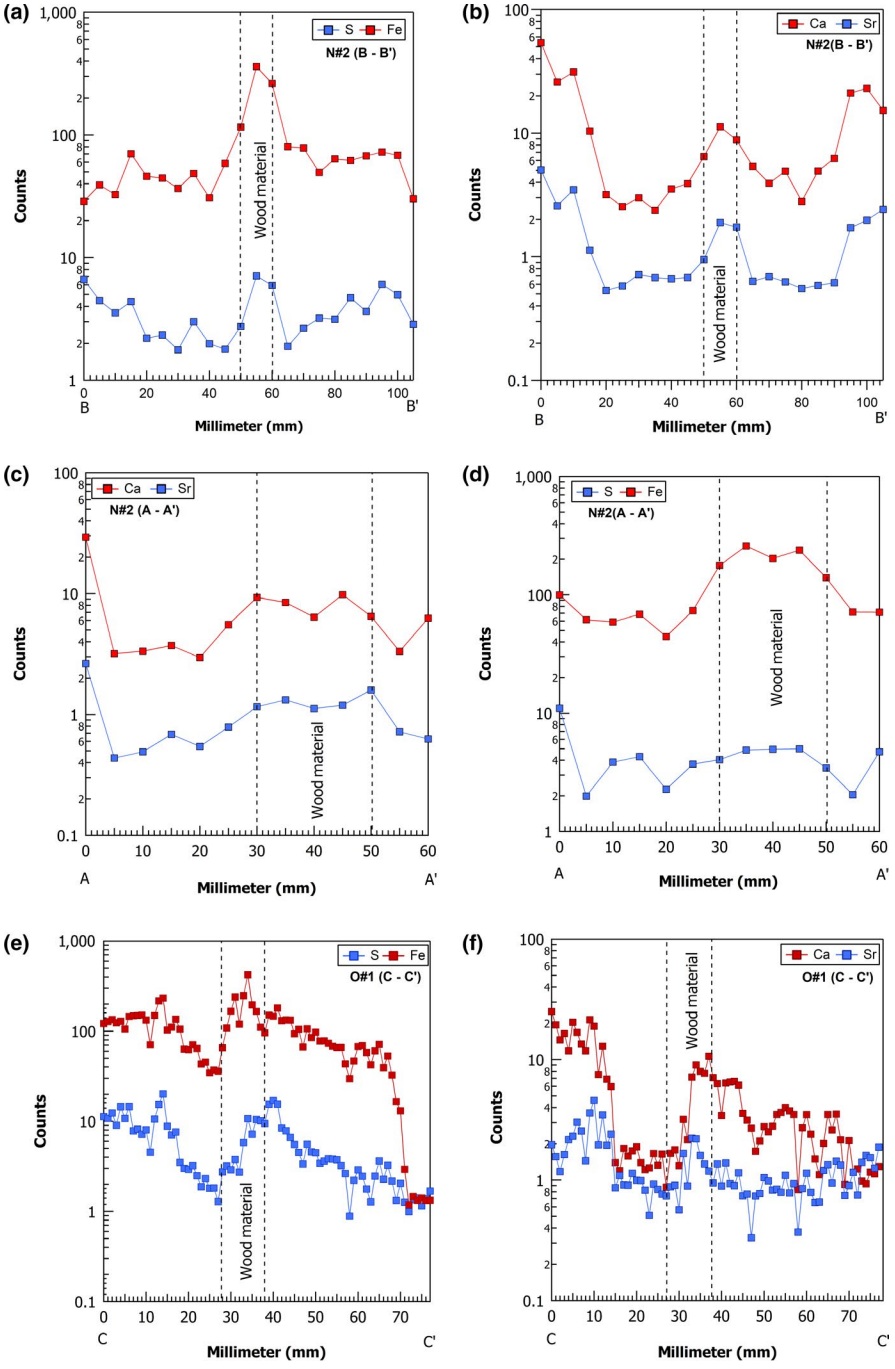

FIGURE 4 Elemental distribution along the cross sections of the concretions (a – f), where the x-axis is the length of concretions in centimeters. Photographs of the transect of A-A' and B-B' from concretion N#2 and C-C' from concretion O#2 are shown in Figure 3. Note that higher resolution of scanning was done across transect C from concretion O#1

visible at the edge of sample N#2. After the concretion has been left open for a day, a black/dark colored region is visible toward the edge of the concretion, whereas a brown/reddish region surrounds the nucleus. The texture of the two concretions is different; O#1 is composed of visible sand-size grains, while N#1 and N#2 are mainly composed of very fine sand, not visible to the naked eye. Biological signatures such as roots and burrows are present in sample O#1. Our XRD analysis indicates the concretions largely comprise siderite, quartz, high-magnesium calcite, orthoclase, albite, and small amount of pyrite (Table 3). Gypsum, greigite, and dolomite were also observed in parts of the concretions in much smaller quantities. Quartz is the dominant mineral (>50%); the remaining contains carbonate minerals such as siderite (6%–27%) and high-magnesium calcite (5%–47%).

The XRF results suggest that the iron content in both concretions is around an order of magnitude higher than the content of calcium or sulfur and two orders of magnitude higher than the content of strontium (Figure 4a,d). Iron content is particularly high in the middle of the concretion but decreases toward the edge of the concretion, while the content of sulfur (without taking the wood material nucleus into account), calcium, and strontium is lowest at the center and increases toward the edge. This is also seen in sample O#1 (transect C–C') where the calcium content drops significantly between 70 and 85 cm, corresponding to the reddish/brownish (sideritic) region of the concretion, whereas high

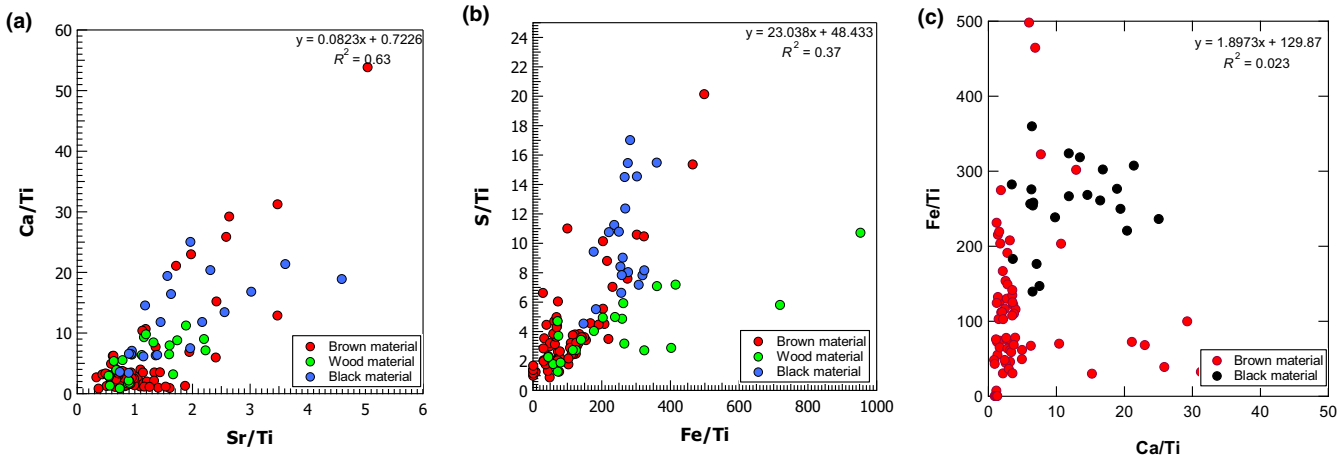

FIGURE 5 Cross-plots with titanium normalized of the studied elements of concretion O#1

TABLE 4 Selected locations (C1–C8) of concretion N#2 with interval approximately 1–2 mm were drilled across from the center to the edge of the concretion for carbon isotope analysis. W1 is wood materials located at the center of the concretion; C9 was sampled near to the edge of the concretion with the darkest and extremely rigid material

Sampling point	$\delta^{13}C_{carb}$ ‰ PDB
W1	-6.45
C1	-1.04
C2	-5.54
C3	-7.86
C4	-12.21
C5	-11.14
C6	-11.58
C7	-12.43
C8	-11.12
C9	-12.31

calcium content is seen in the black (calcite) region (Figure 4f). When we cross plot the XRF data, we see a moderate correlation between calcium and strontium (R^2 = 0.63) (Figure 5). Iron and sulfur are well correlated (R^2 = 0.76) in both concretions excluding the wood. The correlation between iron and sulfur, however, drops dramatically (R^2 = 0.37) when the wood nucleus is included. A weak correlation was found between iron and calcium (R^2 = 0.023) (Figure 5). The final cross plot shows that the brown part of the concretion, closer to the center, is relatively enriched in iron but low in calcium, while the black part of the concretion, close to the outside, has a higher calcium content.

Only one half of the N concretion (N#2) was analyzed for its carbon isotopic composition. Two isotopically distinct regions are found in the N#2 concretion, the isotopically higher inner layer (mean $\delta^{13}C_{carbonate}$ = −4.8‰) and the isotopically lower outer layer (mean $\delta^{13}C_{carbonate}$ = −11.8‰) (Table 4).

4.2 | Incubation experiments with Norfolk sediment

In the incubation experiment, the replicate and control samples show a decrease in alkalinity in the first 50 hr. In the non-control samples, the alkalinity subsequently increases to a maximum of approximately 70 mEq/L before it decreases gradually or remains constant after 400 hr (Figure 6). The pH also increases over the course of the incubation experiments from 6.6 to 7.2. The dissolved (ferrous) iron concentration in the samples increases to 2 mM in the early stage of the incubation then decreases at 200–400 hr.

The sulfate concentration in the samples increases in the early stages of the incubation in both the replicate and control samples. The sulfate concentrations in the live samples started to decrease after 200 hr; this coincides with a decrease in dissolved iron concentration (Figure 6). There is a substantial decrease in sulfate-to-chloride ratio at 400 hr. Sulfide concentrations are relatively low over the course of the incubation. Although the replicate vials start and finish with slightly different sulfate concentrations, the magnitude of change in sulfate concentration is similar. The decrease in sulfate concentration is accompanied by a concurrent decrease in alkalinity and in the concentration of calcium. The solution is initially undersaturated with respect to siderite. The dramatic increase in the $SI_{siderite}$ corresponds to the increase in the concentration of dissolved iron and the increase in alkalinity. The $SI_{siderite}$ then drops to near equilibrium at the onset of microbial sulfate reduction begins before it gradually increases to ~ 1.5 (Figure 6). The control samples have an $SI_{siderite}$ close to equilibrium throughout the experiment.

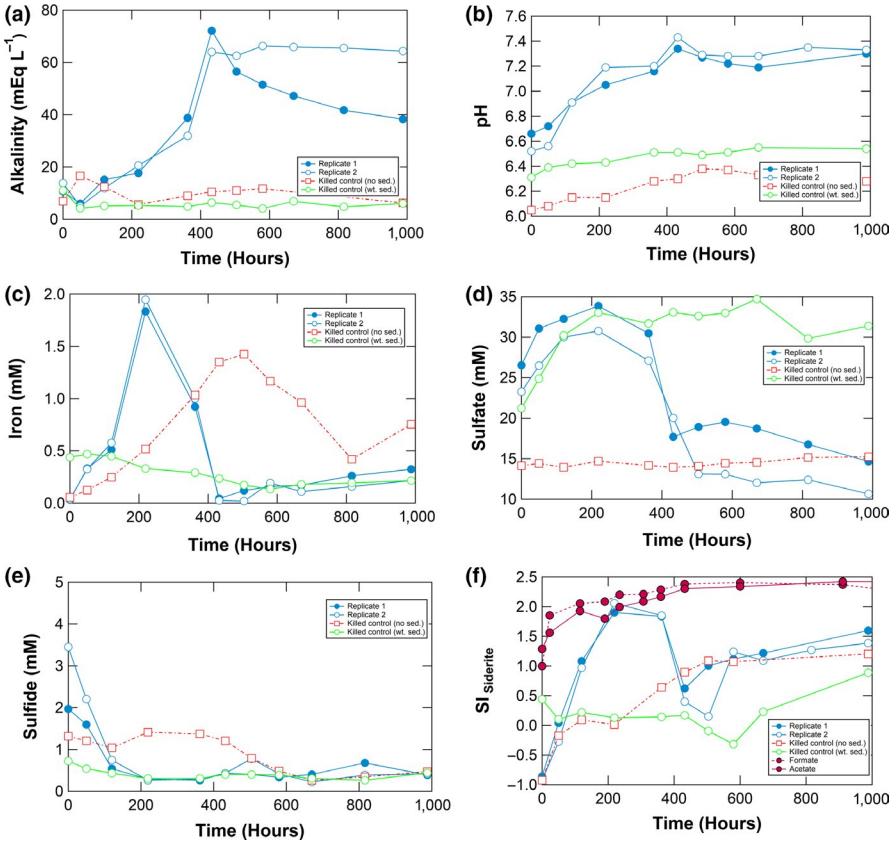

FIGURE 6 Incubation experiment W with plots showing (a) alkalinity; (b) pH; (c) iron; (d) sulfate; (e) sulfide; and (f) saturation index of siderite

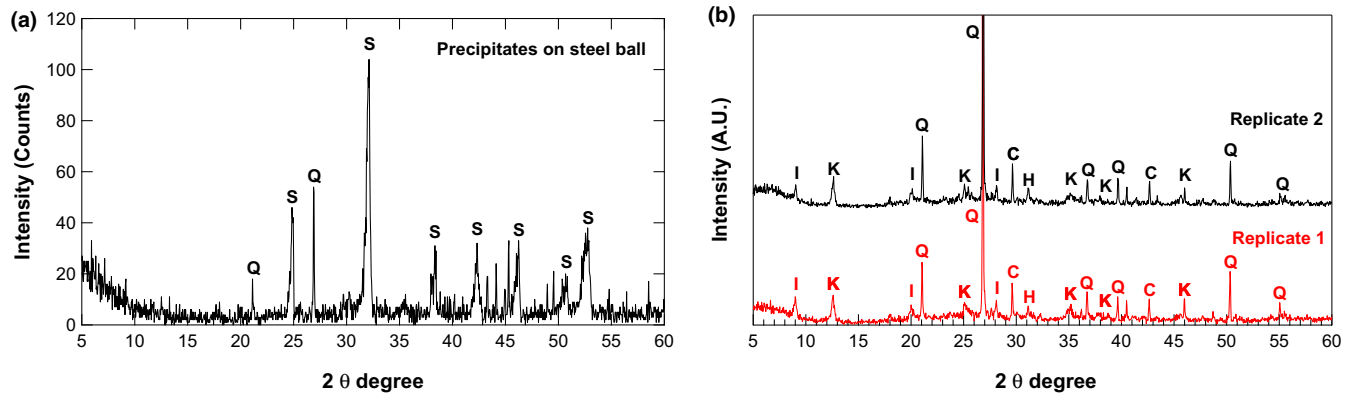

FIGURE 7 Powder X-ray diffraction pattern of the incubation samples (a) outer layer of steel ball; and (b) sediments after the incubation. Q = quartz; S = siderite; K = kaolinite; I = illite; C = calcite. The XRD analysis shows that siderite is only precipitated around steel balls. No siderite is found in the incubated sediment, only calcite

We found a 1 – 2 mm thin layer of black precipitate around the steel ball in the incubated sample (in both replicates 1 and 2—referred as WR1, WR2) (Appendix S1). No precipitate was found on the steel balls of control samples. The black precipitate contains quartz and siderite (Figure 7). When we examined ʻhis precipitate under *SEM*, we note that 1 – 3 μm rhombohedral siderite crystals envelope the steel balls (Figure 8a,b). Elemental mapping shows that the siderite around the steel balls is rich in calcium (Figure 8c,d). The abundance of siderite is low in the surrounding sediment associated with WR1 and WR2 and is not detected by the XRD. However, during *SEM* examination of the bulk sediment we identify some disseminated siderite crystals (Figure 8e). The siderite crystals disseminated in the sediment have a trigonal crystal structure and lower calcium content, different to the one formed around the steel balls in the same samples WR1 and WR2. Despite the absence of a pyrite peak in the XRD pattern of the sediment, we also found framboidal pyrite disseminated in the sediment but in low quantity (Appendix S1).

4.3 | Transformation experiments

Our transformation experiments show that both MHC and calcite will transform to siderite when heated in media containing dissolved iron (Table 5 and Appendix S1). Our results suggest MHC transforms to

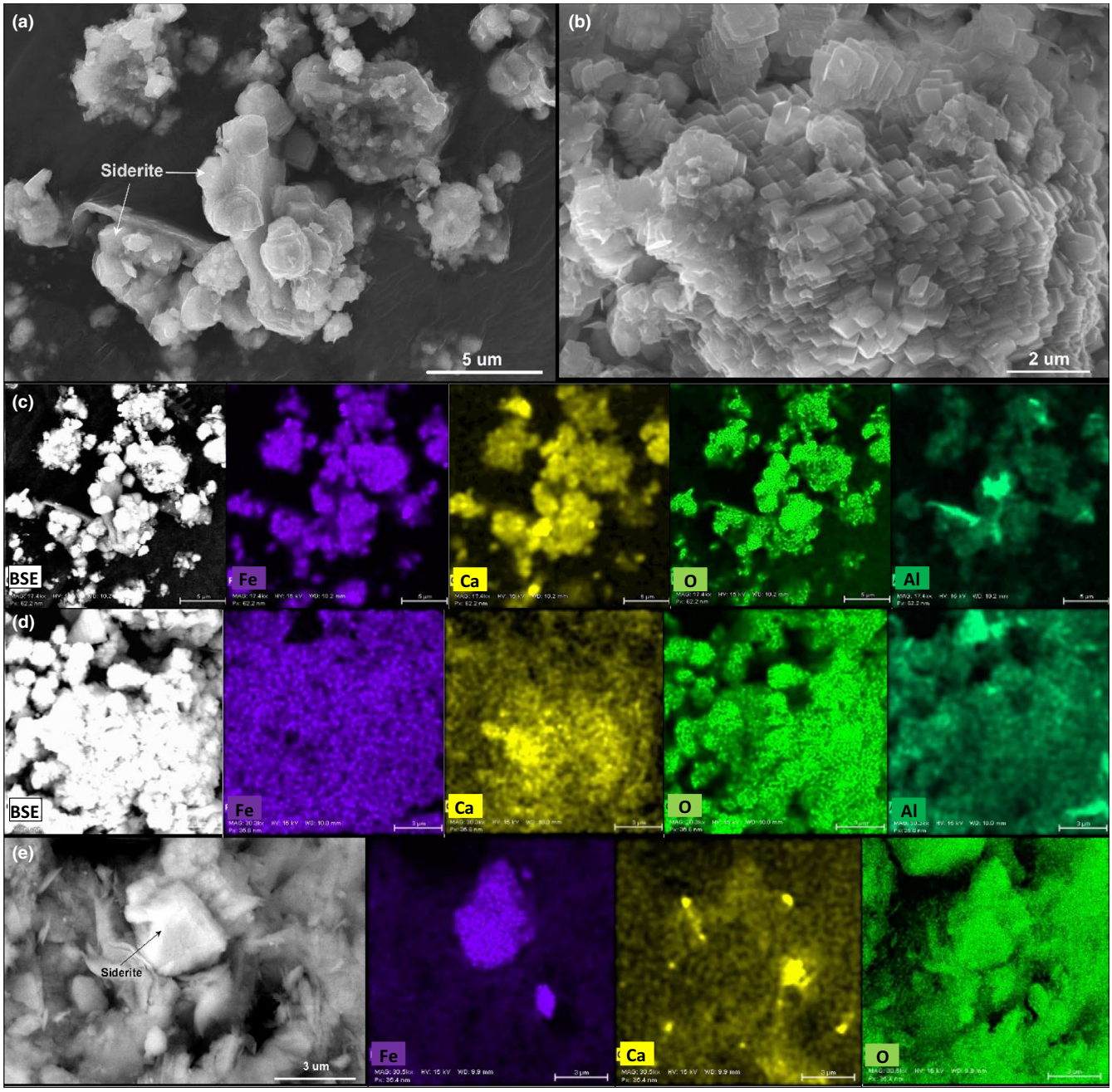

FIGURE 8 (a, b) Secondary electron images and backscatter electron images of siderite collected from the steel balls in WR1 and WR2; (c, d) figures in color show the elemental distribution for iron, calcium, oxygen, and aluminum from WR1 and WR2; (e) trigonal siderite found in replicate one of the WR1 and WR2 sediment. *SEM* image of pyrite found in the sediment is shown in Appendix S1

siderite when the iron concentration in the media was over 40 mM. Calcite transforms to siderite in all samples with initial iron concentrations of 10, 25, 50, and 100 mM (T40–T47) regardless of the medium salinity (MQ or seawater). The amount of siderite formed increases with iron concentration when either calcite or MHC is used in both MQ water and seawater. Universally in samples with MHC seeds, there was less siderite than in the samples with calcite seeds. No carbonate mineral precipitation was found in the seedless control samples (T56–T63) except some rust. The morphology of the formed siderite under *SEM* is large spherulitic aggregates (200 – 300 μm) of rhombohedral shape (Appendix S1). In the samples with calcite seeds, there is a far lower Fe/Ca ratio at the end of the experiment when the transformation is complete (less Fe remaining in solution) than in the samples with the MHC seeds, where the Fe/Ca is quite high (Figure 9).

5 | DISCUSSION

Our primary results are that the siderite concretions appear to have two phases of growth, as evidenced by the change in mineralogy

TABLE 5 Summary of the aqueous chemistry and the final calcium carbonate polymorphs in the transformation experiment. The initial aqueous chemistry of the experiments is given in Table 2. The experiment was carried out in the oven at 100 ˚C for 48 hr except stated otherwise. Rows with common shaded color shared a same initial solution chemistry and were incubated under oxic condition. T32 and T35 are control samples. Samples T40–T63 were incubated under anoxic condition. The initial seed for samples T40–T47 is calcite, while T48–T55 is MHC. Samples T56–T63 are seedless controls. Estimated standard deviation, R_{wp}, and chi-square values for Rietveld quantifications are given in Appendix S1

	Final concentration										Final $CaCO_3$ polymorphs (wt %)						
Samples	pH	Alk (mEq/L)	Ca^{2+} (mM)	Mg^{2+}(mM)	Fe^{2+}(mM) (Initial)	Fe^{2+}(mM) (Final)	PO_4^{3-} (μM)	SO_4^{2-} (mM) §	Mg/Ca	Medium	Final $CaCO_3$	C	Mg-C	MHC	A	V	Sdr
T20(C)*	6.02	8.335	6.02	8.34	50.55	54.75	0.98	<0.01	-	M.Medium	L, Mg-C	-	100	-	-	-	-
T23(C)*	6.07	8.578	6.07	8.58	53.64	59.65	54.64	<0.01	-	M.Medium	-	-	-	-	-	-	-
T26(M)*	6.08	7.828	6.08	7.83	50.55	50.19	1.97	<0.01	-	M.Medium	L, C	100	-	-	-	-	-
T29(M)*	6.42	15.673	6.42	15.67	53.64	59.05	53.26	<0.01	-	M.Medium	C	100	-	-	-	-	-
T32*	1.90	5.238	1.90	5.24	50.55	0.39	0.94	1.01	-	M.Medium	-	-	-	-	-	-	-
T35*	1.55	3.401	1.55	3.40	53.64	9.30	48.16	0.66	-	M.Medium	-	-	-	-	-	-	-
T40[a]	4.33	12.174	80.91	<0.01	98.57	12.42	-	4.33	-	M.Medium	Sdr, C	3.6	-	-	-	-	96.4
T41[b]	5.77	20.530	48.27	0.43	50.63	0.78	-	4.30	0.01	M.Medium	Sdr, C	48.0	-	-	-	-	52.0
T42[c]	5.98	2.593	24.43	0.39	25.78	0.23	-	4.30	0.02	M.Medium	C, Sdr	66.5	-	-	-	-	33.5
T43[d]	6.30	3.505	10.75	0.40	11.03	0.13	-	4.32	0.04	M.Medium	C, Sdr	93.1	-	-	-	-	6.9
T44[e]	5.82	3.363	99.10	52.93	105.04	8.32	-	27.17	0.53	M.Medium	Sdr, C	15.9	-	-	-	-	84.1
T45[f]	6.10	3.728	58.66	54.12	48.74	0.05	-	27.93	0.92	M.Medium	C, Sdr	52.4	-	-	-	-	47.6
T46[g]	6.37	2.971	34.87	53.31	23.67	0.66	-	7.38	1.53	M.Medium	C, Sdr	67.7	-	-	-	-	32.3
T47[h]	6.58	2.807	21.17	54.51	9.74	0.05	-	28.00	2.57	M.Medium	C, Sdr	92.6	-	-	-	-	7.4
T48[a]	5.90	5.664	62.97	1.49	98.57	40.99	-	4.32	0.02	M.Medium	Sdr, C	13.0	-	-	-	-	87.0
T49[b]	6.02	4.344	47.79	1.55	50.63	0.76	-	4.34	0.03	M.Medium	Sdr, C	37.2	-	-	-	-	62.8
T50[c]	6.39	7.009	24.11	1.07	25.78	1.64	-	4.32	0.04	M.Medium	C, Sdr	83.8	-	-	-	-	16.2
T51[d]	6.57	3.685	9.74	0.68	11.03	0.43	-	4.33	0.07	M.Medium	C, Sdr	99.4	-	-	-	-	0.6
T52[e]	6.15	8.567	68.68	54.15	105.04	40.69	-	26.25	0.79	M.Medium	C, MHC, Sdr	3.0	-	30.5	-	-	66.5
T53[f]	6.56	13.436	56.67	52.27	48.74	4.69	-	26.82	0.92	M.Medium	-	-	-	-	-	-	-
T54[g]	6.63	9.833	37.25	48.16	23.67	2.42	-	25.71	1.29	M.Medium	C, A	67.0	-	-	33.0	-	-
T55[h]	6.82	8.918	28.75	44.73	9.74	0.87	-	25.18	1.56	M.Medium	C, A	57.1	-	-	42.9	-	-
T56[a]	2.12	11.904	0.16	<0.01	98.57	101.13	-	4.58	-	M.Medium	-	-	-	-	-	-	-
T57[b]	2.79	12.253	0.17	0.23	50.63	51.83	-	4.53	1.36	M.Medium	-	-	-	-	-	-	-
T58[c]	3.19	11.086	0.16	<0.01	25.78	26.19	-	4.34	-	M.Medium	-	-	-	-	-	-	-
T59[d]	3.75	10.977	<0.01	<0.01	11.03	10.60	-	4.33	-	M.Medium	-	-	-	-	-	-	-

(Continues)

TABLE 5 (Continued)

Samples	Final concentration									Final $CaCO_3$ polymorphs (wt %)						
	pH	Alk (mEq/L)	Ca^{2+} (mM)	Mg^{2+}(mM)	Fe^{2+}(mM) (Initial)	Fe^{2+}(mM) (Final)	PO_4^{3-} (μM)	SO_4^{2-} (mM) [§]	Mg/Ca	Medium	Final $CaCO_3$	C	Mg-C	MHC	A	V	Sdr
T60[e]	2.58	-	10.42	54.03	105.04	88.34	-	26.20	5.19	M.Medium	-	-	-	-	-	-	-
T61[f]	2.79	19.363	10.56	55.24	48.74	48.14	-	27.51	5.23	M.Medium	-	-	-	-	-	-	-
T62[g]	3.13	17.392	10.33	54.22	23.67	23.37	-	27.23	5.25	M.Medium	-	-	-	-	-	-	-
T63[h]	3.46	11.189	10.52	55.15	9.74	6.67	-	28.53	5.24	M.Medium	-	-	-	-	-	-	-

Note: M.Medium = modified medium (medium made up of MQ water/SW) A = aragonite, C = calcite, MHC = monohydrocalcite, Mg-C = magnesium calcite, L = lepidocrocite, V = vaterite, Sdr = siderite. Aqueous samples were measured in duplicates.

*Samples incubated under oxic condition

[§]Estimated values

[a–d] = modified MQ water.

[e–h] = modified SW medium.

within the concretion as well as the change in the carbon isotopic composition of the concretion. Our laboratory experiments suggest that we can form siderite in incubation experiments of the sediment when a steel ball nucleus is added, as well as through heated transformation of pre-existing carbonate seeds, albeit in the presence of high concentrations of iron. In this discussion, we will first consider the microbially induced formation of siderite, and then, we summarize and propose processes that lead to the formation of siderite concretions in the East Anglian salt marsh sediments. We suggest that there may be an ideal condition/window (or "sweet spot") for siderite growth that includes intermittent microbial sulfate reduction, which increases alkalinity and tempers the rise in pH, in a system dominated by bacterial iron reduction, generating an excess of dissolved iron.

5.1 | Siderite formation in the environment and under laboratory experiments

Throughout the salt marsh sediment, we note that siderite does not exceed saturation based on the concentration of DIC and dissolved iron in the sediment beneath the salt marsh ponds (Figure 2). This suggests that the concretions nucleate when the concentration of dissolved iron in the porewater is even higher than has been measured, perhaps in areas of the salt marsh platform where dissolved iron concentrations as much as three times higher have been previously reported (Hutchings et al., 2019). The concretions may then grow further in the majority of the salt marsh sediment where our calculations suggest the $SI_{siderite}$ is closer to unity. The change in the $\delta^{13}C_{carbonate}$ of the siderite concretions reflects a change in the $\delta^{13}C$ of the DIC pool from which the concretion is growing, also supporting the idea that the concretions may nucleate in one position in the salt marsh and grow further in another. The salt marsh platform is a dynamic sedimentary environment, and through sediment accumulation and channel development, salt ponds can develop or become vegetated over a period of less than a decade. If we assume that there is low carbon isotope fractionation on the formation of siderite, our data suggest that the $\delta^{13}C$ of the DIC pool decreases by ~ 7‰ over the growth of the concretion. The $\delta^{13}C$ of DIC in sedimentary pore fluids typically decreases due to the oxidation of organic carbon, which adds ^{12}C-rich carbon to the pore fluid (Irwin, Curtis, & Coleman, 1977). Thus, this change in the $\delta^{13}C$ of the concretion could reflect the depth of concretion growth, where the concretion nucleates closer to the surface where the $\delta^{13}C$ of the DIC is more similar to the overlying pond water ($\delta^{13}C_{DIC}$ = 0‰), and then later grows deeper, where the $\delta^{13}C$ of the DIC has evolved to a lower overall carbon isotope composition. Alternatively, if the depth of concretion growth has not changed, then it could reflect a change the local amount of respired organic carbon or the intensity of local microbial activity. We also note that we cannot rule out possible contamination from organic carbon in the outer layer of the concretion. Organic carbon was not removed prior to analysis; therefore, it is possible that the outer layers of the concretion have more organic material contaminating the carbon isotopic analysis ($\delta^{13}C_{org}$ = −25 to −30‰).

Many carbonate minerals precipitate via less stable carbonate mineral precursors (Blue et al., 2017; Jiang & Tosca, 2019; Lin et al., 2018). Studies of the precipitation and transformation pathways for carbonate minerals allow us to understand how mineralization can be interpreted in the geological record, from the standpoint of the geochemistry and microimaging (Lin et al., 2018). Our transformation experiments suggest that siderite can form from either calcite or MHC (carbonate seeds) when there is the right pH, high iron concentration, and elevated temperature (Table 5 and Appendix S1). Such transformation likely involves two different pathways. In the MHC-seeded samples, we note a lesser decrease in the concentration of dissolved iron (84% less than in the calcite-seeded samples) and lesser increase in the concentration of calcium, which we suggest that the siderite in these samples may have formed via a pathway involving solid-state transformation or ionic replacement/substitution (Table 5, Figure 9). The transformation of MHC to siderite would include the incorporation/replacement of iron for calcium in the MHC lattice, yielding the observed asymmetrical siderite main peak (32˚ angle 2θ) with the peak shifted toward the left (lower 2θ) during XRD (Appendix S1). This peak shift toward the left in the XRD indicates that the siderite incorporates a substantial proportion of ions larger than iron into the crystal lattice—where in this case, calcium is the most plausible due to the lower aqueous calcium concentration measured in the final media. The fact that calcite and aragonite are the dominant minerals formed in the MHC-seeded samples suggests that a dehydration process (removing the lone water from the monohydrocalcite) dominates over this ionic replacement of iron for calcium, especially in solutions with low dissolved iron.

On the other hand, in the calcite-seeded samples, an average of 96% of dissolved iron is removed from the solution during the transformation (Figure 9). Morphological evidence suggests that siderite was formed via the dissolution of calcite and re-precipitation as siderite in the calcite-seeded samples (Figure 10). The nucleation of siderite on calcite seeds possibly starts along the edge of the calcite (at high energy sites such as kinks and steps) and then grows (propagates) toward the middle of the calcite surface (Figure 10). This hints that calcite may be a better seed for siderite formation relative to MHC. Although the iron concentrations in our experiments do not fall within a sensible range found in most surface environments, we think that such a transformation route is plausible over a longer period (because of the slower kinetics). A similar observation has been reported where siderite nucleates and replaces calcite (and ferrihydrite) during hydrothermal carbonate mineralization (Köhler et al., 2013; Pearce, Timmes, Hough, & Cleverley, 2013). The nucleation of microcrystalline siderite on calcite forming a rim also has been documented in a peat marsh environment (McMillan & Schwertmann, 1998).

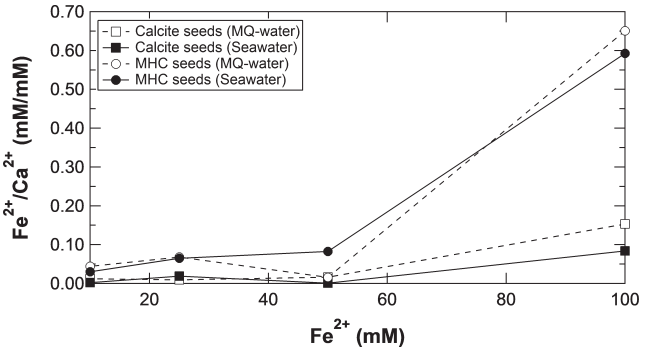

FIGURE 9 The Fe/Ca molar ratio of the aqueous solution collected after the transformation experiment. The x-axis is the initial iron concentration of the samples before transformation experiment. A higher Fe/Ca in the solution indicates more ferrous iron in the dissolved phase, while a lower Fe/Ca suggesting that more iron is removed from the solution via a dissolution and re-precipitation process

5.2 | Formation of siderite in laboratory incubation experiments

Our laboratory incubation experiments suggest that concurrent microbial iron reduction and microbial sulfate reduction start as soon as the incubation was initiated. Both bacterially mediated processes happening simultaneously suggest the microbial community in the East Anglian salt marsh sediments does not follow the conventional redox tower of microbial metabolism, where microbial sulfate reduction occurs when bacterial iron reduction ceases. However, at circumneutral pH, similar to the pH in these salt marshes, the redox tower is more complicated and bacterial iron reduction and microbial sulfate reduction converge on similar free energy yields (Bethke, Sanford, Kirk, Jin, & Flynn, 2011). It is also possible that the sulfate-reducing bacteria we used, *Desulfovibrio desulfuricans*, were

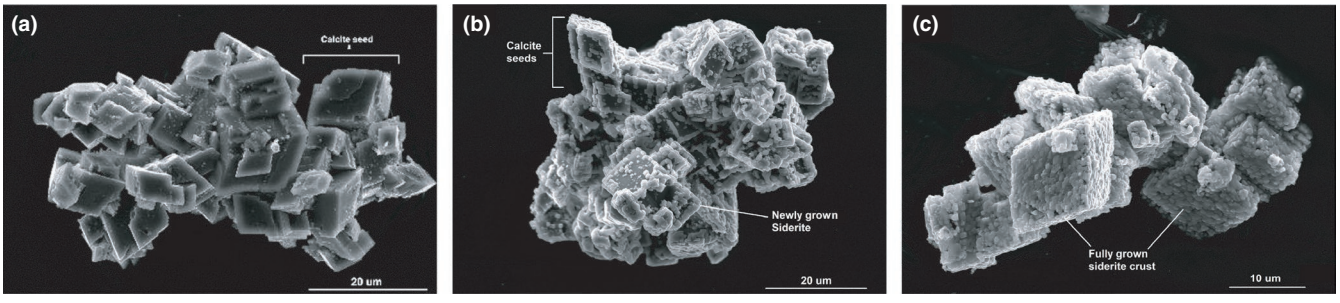

FIGURE 10 Morphological changes in the calcite seeds as siderite precipitated. (a) Original calcite seeds; (b) topotactic nucleation of siderite along the edge and some high energy sites (kinks, steps etc.) of the original calcite seeds; (c) growth of siderite enveloped the calcite seeds

able to reduce iron, causing an inconsistent/ blending respiration of different electron acceptors (Fe and S) (Coleman et al., 1993). In the first 200 hr, the rate of dissolved iron production rate is 0.24 mM/day. The increase in dissolved iron concentration in the killed control sample with the steel ball suggests the release of some dissolved iron from the steel ball. The decrease in iron concentration toward the end of the incubation (after 500 hr) could be due to the precipitation of iron oxides, as we saw ocher and reddish color precipitates in the incubation vial (Figure 6). Microbial sulfate reduction also progresses; however, the process was partially masked by the simultaneous abiotic oxidation of sedimentary sulfide minerals, as evidenced by the increase in sulfate concentration in the killed control samples. The discrepancy in sulfate concentration between the live samples and killed control sample suggests a rate of microbial sulfate reduction of 0.6 mM/day. We suggest that abiotic oxidation of sulfide and microbial sulfate reduction coupled with active microbial iron reduction result in the following equations (Equations 1 – 4):

$$SO_4^{2-} + 2CH_2O \rightarrow 2HCO_3^- + H_2S \quad (1)$$

$$H_2S + 2O_2 \rightarrow SO_4^{2-} + 2H^+ \quad (2)$$

$$4Fe(OH)_3 + CH_2O + 7H^+ \rightarrow 10H_2O + 4Fe^{2+} + HCO_3^- \quad (3)$$

$$4Fe^{2+} + 4HCO_3^- \rightarrow 4FeCO_3 + 4H^+ \quad (4)$$

1. Initially formed hydrogen sulfide is oxidized (by ferric iron or possibly trace amounts of oxygen) (Mortimer et al., 2011) and thus not be able to precipitate all dissolved iron in the system (Equations 1 and 2).
2. Local microbial sulfate reduction generates alkalinity which helps in increasing the ion activity product (specifically the concentration of carbonate ions) for siderite formation (Equations 1 and 3).
3. Active bacterial iron reduction increases the dissolved iron in the system which also increase the ionic activity product (specifically the concentration of dissolved iron) favoring siderite precipitation (Eq. 4).

The above three criteria and Equations 1–4 result in an increase in the concentration of dissolved iron and in the solution alkalinity without the accumulation of sulfide in the system, thus favoring the formation of siderite. This hypothesis agrees with work done by Pye et al. (1990), where they conclude that the formation of authigenic siderite occurs in the zone of microbial sulfate reduction in the East Anglian—specifically Norfolk—salt marsh sediment.

We suggest our laboratory results, which build on the work of Pye et al. (1990), establish criteria for the formation of siderite in the East Anglian salt marsh. However, the fact that siderite concretions are not forming everywhere in the marsh and there is no formation of thick siderite bed/layer suggests that the reactions above are self-limiting, likely by the availability of dissolved iron and the presence and availability of a nucleus. In our incubation experiment, we found a thin layer of siderite precipitated around steel balls, and XRD analysis of the precipitates around steel ball shows asymmetrical siderite peaks, shifted toward lower 2θ, suggest the incorporation of calcium into the lattice of the siderite mineral, increasing the size of the unit cell and the crystal domain. We found that the formation of 2 mm of siderite in our incubation requires a month, while another field study suggested it takes several months to form 10- to 40-μm siderite aggregates (Allison & Pye, 1994). Although the formation of siderite can be rapid (within weeks), the formation and growth of siderite concretions to a centimeter scale are time consuming (months to years) and the kinetics greatly depend on the degree of siderite saturation state (Allison & Pye, 1994; Baird, Sroka, Shabica, & Kuecher, 1986; Clements, Purnell, & Gabbott, 2018; Jiang & Tosca, 2019; Pye et al., 1990; Woodland & Stenstrom, 1979).

In addition, the materials used to seed siderite are important. In our incubations, siderite forms on steel balls and not on wood materials, while an earlier study tried to precipitate siderite on a wider range of nuclei, including calcified arthropod cuticle, non-calcified arthropod cuticle, porous aragonite shell, porous calcite shell, non-porous calcite shell, soft-bodied carcasses, and woody stem material (Allison & Pye, 1994). In that study, siderite was found only in the cavities of oyster shells and cuttlebones (both are aragonite). Field incubation experiments were also reported in Pye et al. (1990), where they found that 0.1- to 2-mm siderite was formed around phosphor bronze, galvanized steel, aluminum, and wood nuclei after six months buried in the East Anglian salt marsh sediment—specifically in the Warham salt marsh. No siderite precipitated on polycarbonate nuclei.

5.3 | Proposed formation of siderite concretion in the marsh

Combining the results from our field and laboratory incubation experiments, we suggest that the formation of siderite concretions in the Norfolk salt marsh sediment begins in a microenvironment where there is a local source of dissolved iron and alkalinity but where the pH is not too high (pH < 7.2). Our incubation results suggest that bacterial iron reduction alone does not generate enough alkalinity to drive siderite saturation and likely would drive the pH too high to make siderite anyway (Figure 6). We suggest that microbial sulfate reduction is needed to provide enough alkalinity for siderite precipitation; however, microbial sulfate reduction has to be maintained at a very low level to prevent the formation of iron-sulfide minerals (Eq. 5, 6).

$$CH_3COO^- + SO_4^{2-} \rightarrow HS^- + 2HCO_3^- \quad (5)$$

$$Fe^{2+} + HS^- \rightarrow FeS_{(s)} + H^+ \quad (6)$$

In addition, dissolution of carbonate minerals such as calcite could also be a possible source for alkalinity as shown in the transformation

experiment. However, the Fe/Ca in the solution has to be poised at a very high ratio (Fe/Ca > 0.2—Berner, 1970; Berner, 1981), which is similar to the Fe/Ca under the salt marsh platform vegetation (Fe/Ca = 0.4–0.6), but not under the salt marsh pond sediment (Fe/Ca = 0.15–0.2—Hutchings et al., 2019). We therefore propose that the siderite concretion formation can be divided into a nucleation and maturation phase in a geochemically dynamic environment and that the East Anglian Salt marshes are a unique environment for siderite concretion formation. During the nucleation stage, bacteria (particularly iron reducing bacteria and at times sulfate-reducing bacteria) start to oxidize the available organic carbon using iron minerals or aqueous sulfate as the terminal electron acceptor. Precipitation of siderite happens when the saturation index of siderite is high and the pore fluid pH is between 6.0 and 7.2. It could be that trace amounts of microbial sulfate reduction, producing hydrogen sulfide which lowers pH, can counteract the high pH generated by only bacterial iron reduction and thus create the ideal conditions or "window" for siderite precipitation and concretion growth.

Our incubation experiments also hint that both bacterial iron and sulfate reduction are at work during the formation of siderite. Our experiments suggest that when catalysts such as steel balls are present, carbonate mineralization can be very rapid (in 2 weeks) and therefore may occur at shallow depth in the marsh (~5 – 20 cm). The preservation of the nucleus in most of the concretions also suggests rapid cementation of siderite minerals within the sediment grains. Within the salt marsh environment, in particular, the brackish water dilutes the calcium and sulfate concentrations from seawater that helps favor supersaturation of iron carbonate minerals over calcium carbonate minerals and promotes the nucleation of siderite. This nucleation stage often cements the grains surrounding the nucleus, forming the inner core of a concretion. The precipitation of siderite in this inner layer depletes the concentration of dissolved iron, which may create a gradient of decreasing iron concentrations away from the center of the concretion. This causes the Fe/Ca to decrease and ultimately toward the edge, impacting further growth of the siderite-rich inner core. The outer core becomes more calcite-rich when the pore fluid Fe/Ca ratio decreases and the precipitation of calcium carbonate is favored over iron carbonate. This leads to the maturation stage of the concretion.

During the maturation stage, the siderite concretion may be buried deeper in the marsh sediment. While in the surface of the East Anglian salt marsh, there is evidence for both bacterial iron reduction (high dissolved iron concentrations, rust precipitates near the surface) and microbial sulfate reduction (a black layer of iron monosulfide minerals found near the surface of the pond sediment as well as beneath the rhizosphere), deeper in the marsh sediment, and both below the rhizosphere and deep in the pond sediment, there is only evidence for bacterial iron reduction and the concentration of DIC is low (Hutchings et al., 2019). This suggests that the concretions must nucleate high in the marsh but when they grow deeper, they may be undersaturated or just at saturation with respect to siderite, and calcite becomes the dominant mineral precipitate. The $\delta^{13}C_{DIC}$ previously reported for the salt marsh pore fluids are consistent with the $\delta^{13}C_{carbonate}$ in the concretion ($\delta^{13}C_{DIC}$ of iron-rich core is −7.0 ‰ PDB; sulfidic core was −13.3 ‰ PDB) (Antler et al., 2019; Pye et al., 1990). Thus, we conclude that the inner core of the concretion is rapidly cemented with mostly siderite, occurring where there is a mixture of bacterial iron reduction and weak microbial sulfate reduction. Our proposed formation pathway, involving locally enhanced alkalinity derived from microbial sulfate reduction, however, is very different from the formation of laminated and disseminated siderite in most lacustrine and marine depositional environments (Heimann et al., 2010; Krylov et al., 2008; Mozley & Wersin, 1992; Vuillemin et al., 2019; Wittkop et al., 2014). Therefore, it should be noted that the formation pathway here is not universal.

6 | CONCLUSIONS

In conclusion, siderite concretions in the East Anglian salt marsh form under active bacterial iron reduction with limited microbial sulfate reduction. Our incubation experiments suggest that bacterial sulfate reduction is needed for the formation of siderite as high alkalinity is required to maintain supersaturation of siderite in the pore fluid. The 2-mm-thick siderite precipitates around the steel ball in the incubated sediment suggest that alkalinity is the limiting factor for siderite minerals to precipitate during bacterial iron reduction while iron is the limiting factor when sulfate reduction begins. Without the increased alkalinity and the presence of effective nucleus, the formation of siderite is unlikely (or delayed) even there is high concentration of iron available. Our suggestion about the requirement of microbial sulfate reduction in siderite formation, however, is largely restricted to marine environments and is not universal. Several studies have reported the formation of siderite concretions without any evidence of microbial sulfate reduction (Köhler, Konhauser, & Kappler, 2010; Krylov et al., 2008).

The formation of siderite and other carbonate minerals via metastable MHC can occur at high temperatures, suggesting the potential of MHC as precursor/intermediate for the formation of other anhydrous phase carbonate minerals via the ionic replacement/substitution route. In contrast, the formation of siderite via calcite follows a different crystallization pathway—that of dissolution and subsequent precipitation. Our transformation experiments suggest that the dissolution of calcium carbonate minerals (particularly calcite) could act as a source for alkalinity to form siderite. In addition, we found that the presence of carbonate seeds serves as an effective nucleation site/precursor for siderite formation. Such a finding could be useful to explain the occurrence of discrete sideritic spots/layers in banded iron formations.

The lack of pyrite and the presence of disseminated siderite in the incubated sediment suggest the heterogeneity of localized geochemistry within the sediment. This could partly explain the occurrence of siderite concretion only in certain microenvironment of the marsh. A Goldilocks point between the degree of iron and sulfate reduction need to be determined in order to make siderite in the marsh sediment. A follow-up experiment with systematic controls is required to fully understand the mechanism of siderite formation.

ACKNOWLEDGMENTS

The authors would like to acknowledge the funding for this research ERC StG 307582 to AVT (CARBONSINK). The authors also benefited from discussion with Tony Dickson. Special thanks also go to Zvika Steiner, Harold Bradbury, Alec Hutchings, Vitaliy Turchyn and Jo Clegg for general discussions and fieldwork support and Giulio Lampronti's help on the X-ray diffraction analysis. CYL would also like to thank the Ministry of Education Malaysia for the SLAI (Skim Latihan Akademik IPTA) scholarship and Universiti Malaya for providing the study leave. AK was supported by grant RSF-19-17-00226.

CONFLICT OF INTEREST

The authors declare no conflict of interest.

ORCID

Chin Yik Lin https://orcid.org/0000-0002-3258-486X
Alexandra V. Turchyn https://orcid.org/0000-0002-9298-2173
Alexey Krylov https://orcid.org/0000-0001-5539-9758
Gilad Antler https://orcid.org/0000-0002-6865-5412

REFERENCES

Abdul Hadi, A. R., & Astin, T. R. (1995). Genesis of siderite in the Upper Miocene offshore Sarawak: Constraints on pore fluid chemistry and diagenetic history. *Geological Society of Malaysia Bulletin*, *37*, 395–413.

Allison, P. A., & Pye, K. (1994). Early diagenetic mineralization and fossil preservation in modern carbonate concretions. *Palaios*, *9*(6), 561–575. https://doi.org/10.2307/3515128

Antler, G., Mills, J. V., Hutchings, A., Redeker, K., & Turchyn, A. V. (2019). The sedimentary carbon-sulfur-iron interplay – a lesson from East Anglian salt marsh sediments. *Frontiers in Earth Sciences*, https://doi.org/10.3389/feart.2019.00140

Bachan, A., & Kump, L. R. (2015). The rise of oxygen and siderite oxidation during the Lomagundi Event. *Proceeding National Academy of Science*, *112*(21), 6562–6567. https://doi.org/10.1073/pnas.1422319112

Baird, G. C., Sroka, S. D., Shabica, C. W., & Kuecher, G. J. (1986). Taphonomy of Middle Pennsylvanian Mazon Creek area fossil localities, Northeast Illinois: Significance of Exceptional fossil preservation in syngenetic concretions. *Palaios*, *1*, 271–285. https://doi.org/10.2307/3514690

Baker, J. C., Kassan, J., & Hamilton, P. J. (1995). Early diagenetic siderite as an indicator of depositional environment in the Triassic Rewan Group, southern Bowen Basin, eastern Australia. *Sedimentology*, *43*, 77–88. https://doi.org/10.1111/j.1365-3091.1996.tb01461.x

Baumann, L. M. F., Birgel, D., Wargreich, M. & Peckmann, J. (2016). Microbially-driven formation of Cenozoic siderite and calcite concretions from eastern Austria. *Australian Journal of Earth Sciences*, *109*(2), 211–232. https://doi.org/10.17738/ajes.2016.0016

Berner, R. A. (1970). Sedimentary pyrite formation. *American Journal of Science*, *268*(1), 1–23. https://doi.org/10.2475/ajs.268.1.1

Berner, R. A. (1981). A new geochemical classification of sedimentary environments. *SEPM Journal of Sedimentary Research*, *51*(2), 359–365.

Bethke, C. M., Sanford, R. A., Kirk, M. F., Jin, Q., & Flynn, T. M. (2011). The thermodynamic ladder in geomicrobiology. *American Journal of Science*, *311*, 183–210. https://doi.org/10.2475/03.2011.01

Blue, C. R., Giuffre, A., Mergelsberg, S., Han, N., De Yoreo, J. J., & Dove, P. M. (2017). Chemical and physical controls on the transformation of amorphous calcium carbonate into crystalline $CaCO_3$ polymorphs. *Geochimica Et Cosmochimica Acta*, *196*, 179–196. https://doi.org/10.1016/j.gca.2016.09.004

Canfield, D. E., Zhang, S., Wang, H., Wang, X., Zhao, W., Su, J., … Hammarlund, E. U. (2018). A mesoproterozoic iron formation. *Proceeding National Academy of Science*, *115*(17), E3895–E3904. https://doi.org/10.1073/pnas.1720529115

Clements, T., Purnell, M., & Gabbott, S. (2018). The Mazon Creek Lagerstatte: A diverse late Paleozoic ecosystem entombed within siderite concretions. *Journal of Geological Society*, *176*(1), 1–11.

Cline, J. D. (1969). Spectrophotometric determination of hydrogen sulfide in natural waters. *Limnology and Oceanography*, *14*, 454–458.

Coelho, W. A. (2007). *TOPAS-Academic*. Brisbane, Australia: Coelho Software.

Coleman, M. L., Hedrick, D. B., Lovley, D. R., White, D. C., & Pye, K. (1993). Reduction of Fe(III) in sediments by sulfate reducing bacteria. *Nature*, *361*, 436–438.

Dickson, A. G., Afghan, J. D., & Anderson, G. C. (2003). Reference materials for oceanic CO_2 analysis: A method for the certification of total alkalinity. *Marine Chemistry*, *80*(2–3), 185–197. https://doi.org/10.1016/S0304-4203(02)00133-0

Dideriksen, K., Frandsen, C., Bovet, N., Wallace, A. F., Sel, O., Arbour, T., … Bandfield, J. F. (2015). Formation and transformation of a short range ordered iron carbonate precursor. *Geochimica Et Cosmochimica Acta*, *164*, 94–109. https://doi.org/10.1016/j.gca.2015.05.005

Dong, H. (2010). Mineral-microbe interactions: A review. *Frontiers of Earth Sciences China*, *4*(2), 127–147. https://doi.org/10.1007/s11707-010-0022-8

Halevy, I., Alesker, M., Schuster, E. M., Popovitz-Biro, R., & Feldman, Y. (2017). A key role for green rust in the Precambrian oceans and the genesis of iron formations. *Nature Geoscience*, *10*, 135–139. https://doi.org/10.1038/ngeo2878

Heimann, A., Johnson, C. M., Beard, B. L., Valley, J. W., Roden, E. E., Spicuzza, M. J., … Beukes, N. J. (2010). Fe, C, and O isotope compositions of banded iron formation carbonates demonstrate a major role for dissimilatory iron reduction in ~ 2.5 Ga marine environments. *Earth and Planetary Science Letters*, *294*, 8–18.

Holland, H. D. (2006). The oxygenation of the atmosphere and oceans. *Philosophical Transactions of the Royal Society of London, Series B, Biological Sciences*, *361*, 903–915. https://doi.org/10.1098/rstb.2006.1838

Hutchings, A. M., Antler, G., Wilkening, J., Basu, A., Bradbury, H. J., Clegg, J. A., … Turchyn, A. V. (2019). Creek dynamics determine pond subsurface geochemistry heterogeneity in East Anglian (UK) salt marshes. *Frontiers in Earth Sciences*, *7*(41), 1-19. https://doi.org/10.3389/feart.2019.00041

Irwin, H., Curtis, C., & Coleman, M. (1977). Isotopic evidence for source of diagenetic carbonates formed during burial of organic-rich sediments. *Nature*, *269*, 209–213. https://doi.org/10.1038/269209a0

Jiang, C. Z., & Tosca, N. J. (2019). Fe(II)-carbonate precipitation kinetics and the chemistry of anoxic ferruginous seawater. *Earth and Planetary Science Letters*, *506*, 231–242. https://doi.org/10.1016/j.epsl.2018.11.010

Köhler, I., Konhauser, K., & Kappler, A. (2010). Role of microorganisms in banded iron formations. In L. L. Barton et al. (eds.), Geomicrobiology: Molecular and Environmental Perspective. DOI: https://doi.org/10.1007/978-90-481-9204-5_14.

Köhler, I., Konhauser, K. O., Papineau, D., Bekker, A., & Kappler, A. (2013). Biological carbon precursor to diagenetic siderite with spherical structures in iron formations. *Nature Communications*, *4*, 1-7. https://doi.org/10.1038/ncomms2770

Konhauser, K. O., Newman, D. K., & Kappler, A. (2005). The potential significance of microbial Fe(III) reduction during deposition of Precambrian banded iron formations. *Geobiology*, *3*, 167–177. https://doi.org/10.1111/j.1472-4669.2005.00055.x

Konhauser, K. O., Planavsky, N. J., Hardisty, D. S., Robbins, L. J., Warchola, T. J., Haugaard, R., … Johnson, C. M. (2017). Iron formations: A global record of Neoarchaean to Paleoproterozoic environmental history. *Earth-Science Reviews*, *172*, 140–177.

Krylov, A., Khlystov, O., Zemskaya, T., Minami, H., Hachikubo, A., Nunokawa, Y., … Pogodaeva, T. (2008). First discovery and formation

process of authigenic siderite from gas hydrate-bearing mud volcanoes in fresh water: Lake Baikal, eastern Siberia. *Geophysical Research Letters*, *35*, L05405. https://doi.org/10.1029/2007GL032917

Lin, C. Y., Turchyn, A. V., Steiner, Z., Bots, P., Lampronti, G. I., & Tosca, N. J. (2018). The role of microbial sulfate reduction in calcium carbonate polymorph selection. *Geochimica Et Cosmochimica Acta*, *237*, 184–204. https://doi.org/10.1016/j.gca.2018.06.019

Liu, R., Liu, F. L., Zhao, S. Q., Su, Y. L., Wang, D. J., & Shen, Q. (2013). Crystallization and oriented attachment of monohydrocalcite and its crystalline phase transformation. *Crystal Engineering Communication*, *15*, 509–515. https://doi.org/10.1039/C2CE26562A

Madsen, I. C., & Scarlett, N. V. Y. (2008). Quantitative phase analysis. In R. E. Dinnabier (Ed.), *Powder diffraction: theory and practice* (pp.298-331). London, UK: Royal Society of Chemistry.

McMillan, S. G., & Schwertmann, U. (1998). Morphological and genetic relations between siderite, calcite and goethite in a low moor peat from southern Germany. *European Journal of Soil Science*, *49*, 283–293. https://doi.org/10.1046/j.1365-2389.1998.00154.x

Mills, J. V., Antler, G., & Turchyn, A. V. (2016). Geochemical evidence for cryptic sulfur cycling in salt marsh sediments. *Earth and Planetary Science Letters*, *453*, 23–32. https://doi.org/10.1016/j.epsl.2016.08.001

Moore, S. E., Ferrell, R. E., & Aharon, P. (1992). Diagenetic siderite and other ferroan carbonates in a modern subsiding marsh sequence. *Journal of Sedimentary Petrology*, *62*(3), 357–366.

Mortimer, J. G. R., Galsworthy, A. M. J., Bittrell, S. H., Wilmot, L. E., & Newton, R. J. (2011). Experimental evidence for rapid biotic and abiotic reduction of Fe (III) at low temperatures in salt marsh sediments: A possible mechanism for formation of modern sedimentary siderite concretions. *Sedimentology*, *58*, 1514–1529. https://doi.org/10.1111/j.1365-3091.2011.01224.x

Mortimer, R. J. G., & Coleman, M. L. (1997). Microbial influence on the oxygen isotopic composition of diagenetic siderite. *Geochimica Et Cosmochimica Acta*, *61*(8), 1705–1711. https://doi.org/10.1016/S0016-7037(97)00027-6

Mortimer, R. J. G., Coleman, M. L., & Rae, J. E. (1997). Effect of bacteria on the elemental composition of early diagenetic siderite: Implications for paleoenvironmental interpretations. *Sedimentology*, *44*, 759–765.

Mozley, P. S., & Wersin, P. (1992). Isotopic composition of siderite as an indicator of depositional environment. *Geology*, *20*, 817–820. https://doi.org/10.1130/0091-7613(1992)020<0817:ICOSAA>2.3.CO;2

Munemoto, T., & Fukushi, K. (2008). Transformation kinetics of monohydrocalcite to aragonite in aqueous solutions. *Journal of Mineralogical and Petrological Science*, *103*, 345–349. https://doi.org/10.2465/jmps.080619

Ohmoto, H., Watanabe, Y., & Kumazawa, K. (2004). Evidence from massive siderite beds for a CO_2 rich atmosphere before ~1.8 billion years ago. *Nature*, *429*, 395–399. https://doi.org/10.1038/nature02573

Pearce, M. A., Timmes, N. E., Hough, R. M., & Cleverley, J. S. (2013). Reaction mechanism for the replacement of calcite by dolomite and siderite: Implications for geochemistry, microstructure and porosity evolution during hydrothermal mineralization. *Contributions to Mineralogy and Petrography*, *166*(4), 995–1009.

Planavsky, N. J., Slack, J. F., Cannon, W. F., O'Connell, B., Isson, T. T., Asael, D., … Bekker, A. (2018). Evidence for episodic oxygenation in a weakly redox-buffered deep mid-Proterozoic ocean. *Chemical Geology*, *483*, 581–594. https://doi.org/10.1016/j.chemgeo.2018.03.028

Pye, K. (1984). SEM analysis of siderite cements in intertidal marsh sediments, Norfolk, England. *Marine Geology*, *56*, 1–12. https://doi.org/10.1016/0025-3227(84)90002-1

Pye, K., Dickinson, A. D., Schiavon, N., Coleman, M. L., & Cox, M. (1990). Formation of siderite-Mg-calcite iron sulphide concretions in intertidal marsh and sandflat sediments, north Norfolk, England. *Sedimentology*, *37*, 325–343. https://doi.org/10.1111/j.1365-3091.1990.tb00962.x

Raiswell, R., & Fisher, Q. J. (2000). Mudrock-hosted carbonate concretions: A review of growth mechanisms and their influence on chemical and isotopic composition. *Journal of the Geological Society, London*, *157*, 239–251. https://doi.org/10.1144/jgs.157.1.239

Roberts, J. A., Kenward, P. A., Fowle, D. A., Goldstein, R. H., Gonzalez, L. A., & Moore, D. S. (2013). Surface chemistry allows for abiotic precipitation of dolomite at low temperature. *Proceeding National Academy of Science*, *110*, 14540–14545. https://doi.org/10.1073/pnas.1305403110

Sanchez-Roman, M., Fernandez-Remolar, D., Amils, R., Sanchez-Navas, A., Schmid, T., Martin-Uriz, P. S., … Vasconcelos, C. (2014). Microbial mediated formation of Fe-carbonate minerals under extreme acidic conditions. *Scientific Reports*, *4*, 4767. https://doi.org/10.1038/srep04767

Sanchez-Roman, M., Puente-Sanchez, F., Parro, V., & Amils, R. (2015). Nucleation of Fe-rich phosphates and carbonates on microbial cells and exopolymeric substances. *Frontiers in Microbiology*, *6*, 1024. https://doi.org/10.3389/fmicb.2015.01024

Sel, O., Radha, A. V., Dideriksen, K., & Navrotsky, A. (2012). Amorphous iron (II) carbonate: Crystallization energetics and comparison to other carbonate minerals related to CO2 sequestration. *Geochimica Et Cosmochimica Acta*, *87*, 61–68. https://doi.org/10.1016/j.gca.2012.03.011

Soetaert, K., Hofmann, A., Middleberg, J., Meysman, F., & Greenwood, J. (2007). The effect of biogeochemical processes on pH. *Marine Chemistry*, *105*, 30–51. https://doi.org/10.1016/j.marchem.2006.12.012

Stookey, L. L. (1970). Ferrozine – a new spectrophotometric reagent for iron. *Analytical Chemistry*, *42*, 779–781. https://doi.org/10.1021/ac60289a016

van Lith, Y., Warthmann, R., Vasconcelos, C., & McKenzie, J. A. (2003). Sulfate-reducing bacteria induce low-temperature Ca-dolomite and high Mg-calcite formation. *Geobiology*, *1*, 71–79.

Vuillemin, A., Wirth, R., Kemnitz, H., Schleicher, A. M., Friese, A., Bauer, K. W., … Vogel, H. (2019). the Towuti Drilling Project Science Team. *Geology*, *47*, 540–544.

Wittkop, C., Teranes, J., Lubenow, B., & Dean, W. (2014). Carbon- and oxygen-stable isotopic signatures of methanogenesis, temperature, and water column stratification in Holocene siderite varves. *Chemical Geology*, *389*, 153–166. https://doi.org/10.1016/j.chemgeo.2014.09.016

Woodland, B. G., & Stenstrom, R. C. (1979). The occurrence and origin of siderite concretions in the Francis Creek shale (Pennsylvanian) of Northeastern Illinois. *Mazon Creek Fossils*, *69*–103.

Xiouzhu, Z., Unfei, W., & Huaiyan, L. (1996). Authigenic mineralogy, depositional environments and evolution of fault-bounded lakes of the Yunnan Plateau, south-western China. *Sedimentology*, *43*, 367–380. https://doi.org/10.1046/j.1365-3091.1996.d01-10.x

Zachara, J. M., Fredrickson, J. K., Li, S.-M., Kennedy, D. W., Smith, S., & Gassman, P. L. (1998). Bacterial reduction of crystalline Fe^{3+} oxides in single phase suspensions and subsurface materials. *American Mineralogist*, *83*, 1426–1443.

Zeng, Z., & Tice, M. M. (2014). Promotion and nucleation of carbonate precipitation during microbial iron reduction. *Geobiology*, *12*, 362–371. https://doi.org/10.1111/gbi.12090

SUPPORTING INFORMATION

Additional supporting information may be found online in the Supporting Information section.

How to cite this article: Lin CY, Turchyn AV, Krylov A, Antler G. The microbially driven formation of siderite in salt marsh sediments. *Geobiology*. 2020;18:207–224. https://doi.org/10.1111/gbi.12371